Enabling 4C Fast Charging of Lithium-ion Batteries by Coating Graphite with a Solid-State Electrolyte

Eric Kazyak[‡], Kuan-Hung Chen[‡], Yuxin Chen, Tae H. Cho, Neil P. Dasgupta*

Dr. Eric Kazyak, Yuxin Chen, Tae H. Cho, Prof. Neil P. Dasgupta

Department of Mechanical Engineering, University of Michigan, Ann Arbor, MI, 48109
E-mail: ndasgupt@umich.edu

Dr. Kuan-Hung Chen, Prof. Neil P. Dasgupta
Department of Materials Science and Engineering, University of Michigan, Ann Arbor, MI, 48109

[‡]These authors contributed equally

Abstract

Enabling fast-charging ($\geq$4C) of lithium-ion batteries is an important challenge to accelerate the

adoption of electric vehicles. However, the desire to maximize energy density has driven the use of

increasingly thick electrodes, which hinders rate capability. Herein, atomic layer deposition was used

to coat a single-ion conducting solid electrolyte (Li_3BO_3-Li_2CO_3) onto post-calendered graphite

electrodes, forming an artificial solid-electrolyte interphase (SEI). When compared to uncoated

control electrodes, the solid electrolyte coating: 1) eliminates natural SEI formation during preconditioning; 2) decreases interphase impedance by >75% compared to the natural SEI; and 3) extends cycle life under 4C charging conditions, enabling retention of 80% capacity after 500 cycles (compared to 12 cycles in the uncoated control) in pouch cells with >3 mAh-cm^{-2} loading. This work demonstrates that 4C charging without Li plating can be achieved through purely interfacial modification without sacrificing energy density, and sheds new light on the role of the SEI in Li plating and fast-charge performance.

1. Introduction

Lithium-ion batteries (LIBs) have become a vital part of the way that society stores and uses electrical energy. Among the myriad applications, electric vehicles (EVs) are rapidly becoming the dominant source of demand for rechargeable batteries.[1] Despite significant advances over the past several years, further improvements in energy density, charging rate, and cycle life remain key challenges.[2] In particular, achieving all of these characteristics simultaneously is elusive.

Tradeoffs arise between energy density, charging rate, and cycle life when thicker (higher areal capacity) electrodes are used.[3] This has been largely attributed to mass-transport limitations in the electrolyte within the porous electrode structures, which lead to increased cell polarization, current focusing, and inhomogeneous lithiation.[4,5] As a result, metallic Li can plate out on the graphite anode surface under fast-charging conditions in high-energy-density cells. The irreversibility associated with Li plating leads to permanent loss of Li from the accessible reservoir and capacity fade, which is the key challenge that limits fast-charging of LIBs.

Strategies to prevent and/or mitigate the impacts of Li plating on graphite have drawn great interest in recent years, including: 1) alternative anode materials such as lithium titanate,[6] titanium niobate,[7] and hybrid mixtures of hard carbon with graphite;[5] 2) modifying the electrode architecture to facilitate enhanced mass transport;[8–12] 3) asymmetric temperature modulation;[13] 4) surface coatings to modify interface behavior;[14–17] and 5) electrolyte modifications to increase ionic conductivity.[18–20] To date, a majority of work on fast charging of graphite aims to homogenize the current distribution throughout the electrode thickness by improving mass transport in the electrolyte.

While these works have shown great promise for enabling fast charging and have demonstrated the importance of mass transport, less attention has been paid to the role of the solid-electrolyte interphase (SEI) in determining fast-charge performance. In state-of-the-art LIBs, a composite SEI consisting of a mosaic of inorganic and organic species forms naturally during the initial charge due to electrolyte decomposition as the graphite electrode potential drops towards the equilibrium potential of Li metal (-3.04 V vs. SHE).[21–23] The primary means of engineering the SEI has been through electrolyte modifications, which has proven to be a key enabler for the high Coulombic efficiency and long cycle-life of today's LIBs.[24] The properties of the natural SEI are sufficient to enable stable cycling at low current densities, when the electrochemical potential remains >0 V vs. Li/Li+, but do not prevent Li plating during fast-charging.

While artificial SEI (a-SEI) coatings have been studied to improve interfacial stability, less attention has been paid to optimization of a-SEIs for fast charging and suppression of Li plating. Our hypothesis in this work is that an ideal a-SEI for fast charging would: 1) have higher ionic conductivity than the natural SEI and low electronic conductivity; 2) be chemically homogenous, avoiding "hot-

3

spots" within the SEI such as grain boundaries, local variations in composition and phase, etc.; 3) be electrochemically stable both in contact with the liquid electrolyte and with Li metal, such that decomposition reactions do not occur even below 0 V vs. Li/Li$^+$; and 4) suppress both natural SEI formation and Li plating.

Fortunately, there has been a great deal of recent work to understand solid electrolyte materials that are stable in contact with Li metal,[25] and nucleation behavior in Li metal anodes.[26] Motivated by this work in the solid-state battery community, we have recently developed atomic layer deposition (ALD) processes for single-ion conducting solid electrolytes that are stable against Li.[27,28] In particular, ALD glassy Li$_3$BO$_3$-Li$_2$CO$_3$ (LBCO) solid electrolytes exhibit the properties listed above. LBCO films were shown to have the highest measured ionic conductivity of any ALD film reported to date (>2*10^{-6} S/cm at 30 °C), and are stable when cycled in contact with Li metal.[29] LBCO materials have also previously been demonstrated as an artificial interphase in sulfide solid state batteries to improve interface stability and improve rate performance.[30]
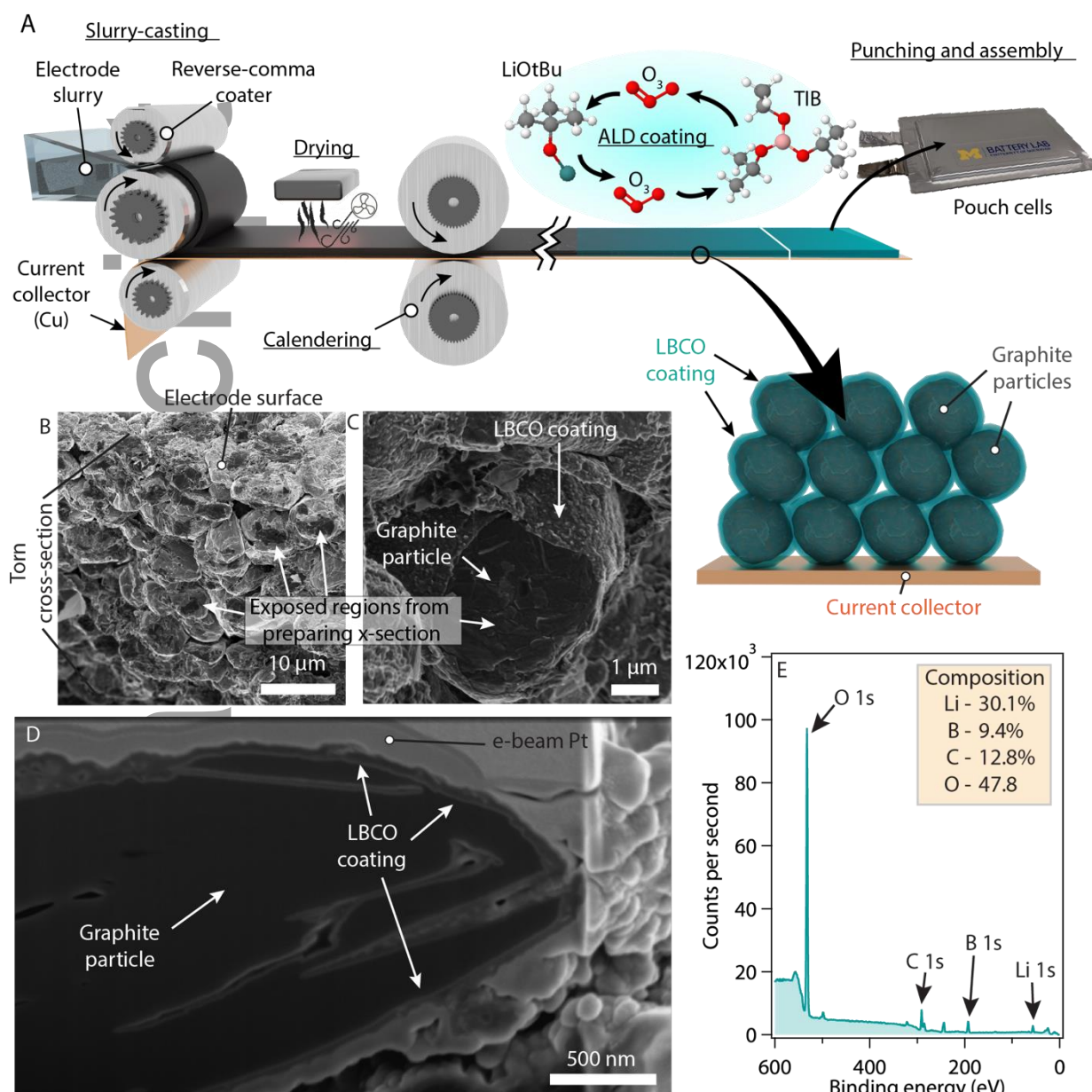
ALD affords unparalleled control of film thickness and conformality owing to the self-limiting nature of the surface reactions.[31] ALD is a powerful means of interface modification for electrode materials in LIBs,[32–41] but work to date has largely focused on coating cathodes to improve interface stability.[42–44] Reports of coatings on graphite have been limited to Al$_2$O$_3$[32,33,35,45] and TiO$_2$,[34,45] and have generally been extremely thin, often less than 1 nm. This is due to the fact that these oxide materials are relatively poor ionic conductors, even after they are electrochemically lithiated, which consumes Li.[46] In addition, the impact of ALD coatings on Li plating during fast charging of LIBs has not been previously studied.

A summary of previous work on modified graphite electrodes for fast-charging is provided in **Table S1**. Much of the previous work, particularly on artificial SEIs, has not focused on Li plating, and did not conduct extended fast-charge cycling in full cells with cathode materials to quantify capacity retention. There are also relatively few examples that used commercially-relevant graphite loadings (>3 mAh/cm^2), where Li plating is expected to be the largest barrier to fast-charging performance.

Herein we demonstrate the use of a single-ion conducting solid electrolyte (LBCO) coating on graphite. The conformal ALD coating is shown to eliminate natural SEI formation, resulting in a 75% decrease in interphase impedance. Cells with coated electrodes exhibit superior rate capability and stability during fast charging. The cycle life to 80% capacity retention under 15 minute (4C) fast-charging conditions was increased to 500 cycles, compared to 12 for uncoated control cells. This is primarily attributed to the suppression of Li plating. In addition to demonstrating a new strategy to overcome energy/power density tradeoffs, this work points to the key role of the SEI and its associated impedance in limiting the fast-charge capability of LIBs.

2. Results and Discussion

Graphite electrodes were prepared on a pilot-scale roll-to-roll slurry-casting system at the University of Michigan Battery Manufacturing Lab via the process shown in **Figure 1a** (further details in Experimental methods).[5,9] To demonstrate that the LBCO ALD process could successfully coat post-

calendered graphite electrodes, x-ray photoelectron spectroscopy **Figure 1. Demonstration of LBCO**

ALD coating approach for graphite electrodes. (A) Schematic of the electrode fabrication process

including slurry-casting, calendering, ALD, and cell assembly. (B,C) SEM images of a torn cross-

section of LBCO 500x coated graphite electrode. (D) SEM image of focused-ion beam cross-section

through a single graphite particle showing the conformal LBCO encapsulation of the particle. (E) XPS survey scan and calculated composition of 250x LBCO-coated electrode surface.

(XPS) and scanning electron microscopy (SEM) were performed after the coating process. Figure 1b shows an XPS survey scan of a graphite electrode surface coated with 250 ALD supercycles of LBCO (~20 nm). One supercycle consists of sequential exposures of lithium tert-butoxide, ozone, triisopropylborate, and ozone, each separated by purging, as described previously.[29] This will be termed LBCO 250x throughout the manuscript, and other

thicknesses will be described similarly based on the number of ALD cycles. As expected for the LBCO coating, the surface is composed of lithium, carbon, boron, and oxygen, and the peak positions match those for the glassy LBCO phase (Figure S3), which has been shown to be amorphous using synchrotron XRD.[29]

SEM imaging was performed on an LBCO-coated electrode to observe the morphology and conformality of the ALD coating. As shown in Figure 1c, the presence of a surface coating can clearly be observed, along with the exposed regions of the electrode that resulted from tearing of the electrode to prepare the cross-section. While the entire surface of the electrode particles was conformally coated, when the electrode was torn to create a cross-section, the contact points between adjacent graphite particles resulted in these exposed regions. These point contacts show that the particle-particle contacts formed during the calendaring process are maintained after coating, preserving electrical continuity throughout the electrode. The conformality of the film

7

through the full thickness of the electrode, together with the electrochemical results shown in

Figure 2, confirm that the ALD process successfully coated the entire electrode.

A high-magnification SEM image of a focused-ion beam (FIB) cross-section is shown in Figure 1d. The film is ~40 nm thick, as expected for the 500x coating, and conformally coats along the entire surface of the graphite particle, including re-entrant surface geometries and the bottom surface that would be shadowed when using line-of-sight deposition methods. This type of conformal coating with precisely controllable thickness would be challenging to achieve with other coating techniques, demonstrating the unique properties of ALD for
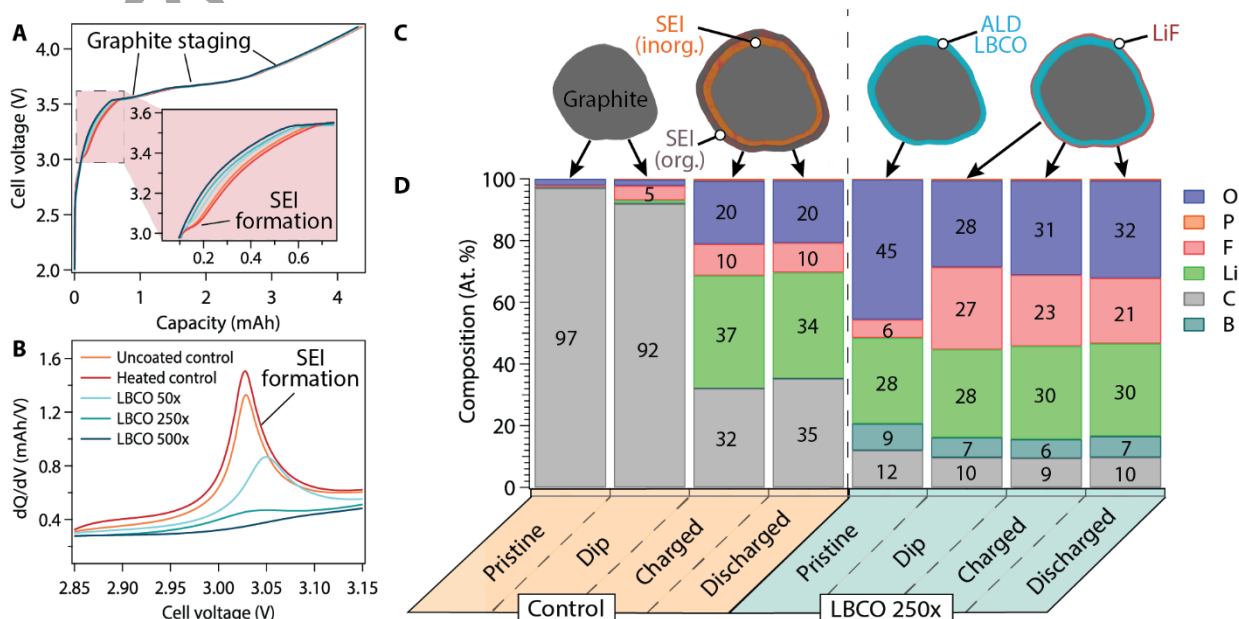
coating of electrode materials.

Figure 2. SEI formation during first preconditioning cycle. (A) Charge curve for first preconditioning cycle of graphite-NMC532 coin cells with varying thicknesses of the LBCO coating on the graphite electrode. (B) Differential voltage curves corresponding to the SEI formation plateau in (A). (C) Schematic of the surface film evolution during

preconditioning for control and LBCO 250x electrodes. (D) Composition of electrode surface at various stages of preconditioning as measured by XPS after 60 seconds of Ar sputtering to reduce adventitious species.

To investigate any physical changes to the electrodes that might have been caused by the elevated temperatures or vacuum conditions during the ALD process, the thickness and mass of multiple control (no exposure to the ALD chamber), heated control, and LBCO 250x coated electrodes were measured. The heated control was exposed to the temperature and pressure conditions of the ALD reactor for the same length of time as the 250x process. The resulting measurements are shown in Figure S1, which indicate that the total thickness of the calendared graphite electrodes increased by approximately 4-8% due to the ALD temperature and pressure conditions. SEM analysis of the electrodes before and after LBCO coating was performed to compare the electrode microstructure (Figure S2). No significant differences in pore size, porosity, or particle size were observed. To exclude any potential effects from these slight structural changes on the observed electrochemical behavior, we also examine the performance of the heated control without ALD coating below.

2.2. Suppression of SEI formation during preconditioning

Graphite electrodes (3.18 mAh-cm^{-2} loading, details in Experimental Methods) were prepared with varying numbers of ALD cycles (50x, 250x, and 500x corresponding to 4, 20, and 40 nm) to investigate the impact of the ALD coating on cell performance and identify the optimal thickness. The electrode loading was chosen to strike a balance between energy density and power density. At this loading, we have previously shown that Li plating is the primary cause of capacity fade under fast-charge conditions.[9] These electrodes were assembled into coin cells with NMC532 cathodes for testing (details in Experimental Methods).

After assembly, the cells were preconditioned with (3) C/10 constant current (CC) cycles, the first of which is shown in Figure 2a. The first plateau in the first charge (observed at ~3.0 volts) is associated with the initial SEI that forms on the graphite surface as the potential of the electrode drops below the reductive stability limit of the electrolyte.[24,47] This plateau, which appears as a peak in the dQ/dV plot (Figure 2b), decreases with increasing thickness of LBCO coating. The plateau is almost completely suppressed in the 250x sample and is absent in the 500x sample. This indicates that when the LBCO coating is sufficiently thick, it passivates the surface of the graphite by blocking electron transport, preventing reductive side-reactions with the salt and solvents that lead to SEI formation and growth. This is possible due to the wide electrochemical stability window of the LBCO solid electrolyte film,[29] which prevents reductive decomposition of the coating at the potentials where natural SEI formation normally occurs. The suppression of electrolyte decomposition not only enables superior control over interphase properties, but could alleviate the need for preconditioning cycles in a manufacturing setting. This is one of the most costly and time-consuming steps during battery manufacturing, due to the very slow charging rates used, and the large footprint required for equipment.[48]

Further insights into the differences in the SEI formation process were acquired via XPS analysis of both the control and 250x electrodes at various stages of formation: 1) pristine; 2) dipped in electrolyte; 3) after charging to 4.2V (charged); and 4) after one full cycle (discharged). These data, shown in Figure 2d, show substantial differences in the surface chemistry as the formation cycle proceeds. The pristine control electrode is comprised almost entirely of carbon, while the 250x coating closely resembles the LBCO film composition (Figure 2D). A small amount of adventitious fluorine is present, which results from exposure to electrolyte vapors in the glovebox environment.

After submersing the electrode in the liquid electrolyte for 30 minutes and rinsing with dimethyl carbonate (DMC), the control electrode was still comprised of >90% carbon, with a modest increase in the amount of fluorine present. Examination of the F 1s core scan (Figure S4), reveals that this F content arises from residual $LiPF_6$ salt, rather than a reacted interphase. In comparison, the 250x LBCO electrode exhibited a relatively higher increase in F content, most of which was LiF in character based on the core scans. This indicates that the LBCO ALD film chemically reacts with the electrolyte under open circuit conditions. The spontaneous formation of LiF under open circuit conditions has been previously been shown in similar electrolyte systems, and was attributed to surface-dependent catalytic reduction of electrolyte species.[49] In the future, computational studies will be valuable to further elucidate this mechanism on the LBCO surface. Notably, the resulting surface did not increase in C content after the electrolyte exposure, indicating that solvent decomposition does not occur on the LBCO surface. Furthermore, the B content only slightly decreases, and does not experience a chemical shift (Figure S5). This demonstrates that an ultrathin LiF layer is present on the surface of the LBCO coating, which is significantly less than the escape depth of the photoelectrons emitted from LBCO. The thickness of LiF was calculated to be approximately 1 nm based on the Electron Effective-Attenuation Length Calculator from the National Institute of Standards and Technology (Table S2).[50] Therefore, the a-SEI is composed of the single-ion conducting LBCO solid electrolyte, with an ultrathin LiF surface layer (Figure 2C). Both of these materials exhibit a wide electrochemical stability window, which prevents natural SEI formation under reductive conditions.

Following the first C/10 charging half-cycle, the surface composition of the control electrode changed dramatically. The carbon content of the control decreased from 92% to 32%, while the Li

content increased from nearly zero to 37%, the O increased from near zero to 20%, and the F increased from 5% to 10%. These changes are consistent with the natural SEI formation that forms as the potential of the graphite electrode is decreased below the reductive stability window of the electrolyte during lithiation.[47]

In contrast, the 250x LBCO electrode surface composition was nearly identical to the dipped sample, illustrating that the LBCO electrode prevented natural SEI formation. After discharging the cell, neither the control or the 250x LBCO electrode exhibited substantial changes, although the control did decrease in Li content slightly.

The improved electrochemical stability of the 250x LBCO electrode compared to the control is consistent with the voltage curve analysis in Figure 2a-b. This is also consistent with cyclic voltammetry data for ALD LBCO, which do not show reductive currents as the electrode potential is decreased within the range of natural SEI formation.[29] These results illustrate the benefits of using a solid-state electrolyte with a wide electrochemical stability window to provide several of the properties of an "ideal" a-SEI that were listed above.

2.3. Improved fast-charging performance

To study the influence of the a-SEI thickness on cycling performance and fast-charging capability, coin cells were subjected to various charging rates and extended cycling at a 4C rate (Further details in Supplementary Information, Figure S6). 4C fast charging has been identified by the U.S. Department of Energy (DoE) and U.S. Advanced Battery Consortium (USABC) as a target metric for EV batteries, and thus was used as the primary charging rate in this work. The 250x coating had the

best performance in terms of capacity retention, and thus was selected as the optimal coating thickness for the remainder of the study.

To investigate cell performance in a more industrially-relevant format, single-layer pouch cells (70 cm² electrodes) were fabricated for the control and the optimal 250x LBCO coating. The stack-specific energy density of these cells at C/3 was 228 Wh/kg (further details in the Supporting Information, Figure S7). Extended cycling with 4C fast charging was performed, following the U.S. DoE test protocol for fast charging (further details in Figure 3 caption).[5,51] Consistent with this test protocol, the accessible capacity at low charge rate was also checked every 50 cycles. As shown in **Figure 3**, the control cells exhibit rapid capacity fading in the first 10-20 cycles before reaching a more stable aging condition. The rapid capacity fade in the initial cycles of the control corresponds to a dip in the Coulombic efficiency (CE), which has been shown to be a result of Li plating.[9] This irreversibility depletes Li from the active reservoir, resulting in the capacity fading observed in Figure 3. The driving force for additional Li plating is reduced with the loss of lithium inventory, and thus the capacity retention at the end of the tests approaches a plateau value, consistent with previous studies.[3,9,52,53] As a result, the capacity retention at C/3 is 67.3% after 50 4C-charge cycles. In contrast, the CE of the LBCO 250x cells is consistently higher than the controls, and do not exhibit the initial dip in CE. The LBCO 250x cells exhibit significantly less capacity fade, retaining 89.5% of the original capacity to 50 cycles, and 79.4% after 500 cycles (Figure 3b).

The plot in Figure 3d shows only the cycles with 4C fast-charging (without the periodic capacity checks). Compared to the accessible capacity of the initial 4C charge cycle, the control cell fades to 80% capacity after only 12 cycles. In comparison, the LBCO 250x

retains more than 80% capacity throughout the 500-cycle test. This represents a greater than 40-fold

increase in cycle life.

Further insights can be gained by examining the charge curves for the 1st and 100th fast-

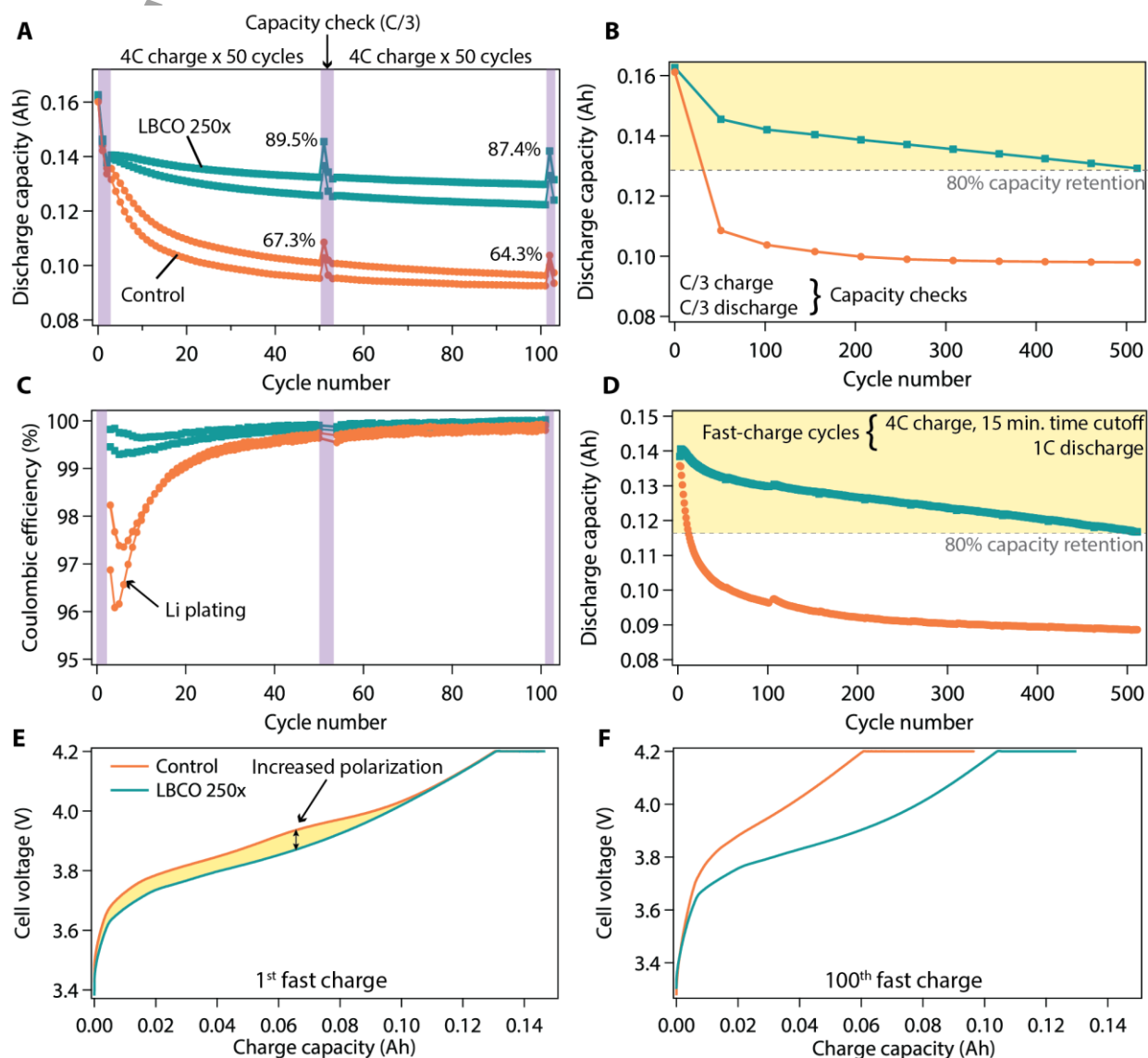charge cycles, shown in Figure 3e and 3f, respectively. During the first 4C charge, the

Figure 3. Extended cycling of NMC532/graphite pouch cells with and without LBCO coating. (A) Discharge capacity for each cell over the first 100 fast-charge cycles and 3 capacity checks. Two replications are shown for each treatment. Labelled values are the

higher of the two cells for each treatment. Cycling data for additional cells and treatments are shown in Figure S11. (B) Discharge capacity for only periodic C/3 capacity-check cycles over 500 total fast-charge cycles. The 80% line is based on the initial C/3 capacity check (C) Coulombic efficiency values for fast-charge cycles in (A). Data points for the capacity checks and the subsequent fast-charge cycles were omitted due to changes in charge/discharge rates which cause unmeaningful CE values. (D) Discharge capacity for 4C fast-charge cycles only. 80% line is based on initial fast-charge cycle. (E) Charge curve for first 4C charge and (F) Same for 100th 4C charge. For all 4C cycles, a constant current (CC) was applied until a cutoff voltage of 4.2 V, followed by a constant voltage (CV) hold until the total time for the charging step reached 15 minutes.

control electrode exhibits a higher cell voltage, and this remains the case throughout cycling. As shown in Figure S8, the voltage traces at a C/10 rate are nearly identical. Therefore, the higher cell voltage in the control is a result of larger polarization under fast-charge conditions. This indicates that the LBCO coating reduces the cell impedance, which is analyzed in detail in the following section. After 100 cycles (Figure 3f), the capacity of the control cell has faded dramatically, and the cell voltage quickly hits the 4.2 V cutoff. In the LBCO 250x cell, the accessible capacity within the CC portion of the charge is nearly double that of the control, and it retains a larger fraction of the initial capacity.

The decreased polarization in the LBCO cell also results in a higher energy efficiency (the ratio of energy delivered by the cell during discharge to energy input during charging), particularly during fast charging. As shown in Figure S9, the energy efficiency of the LBCO cell is higher throughout cycling, and does not exhibit the dip in the early stages that is observed for the control that corresponds with Li plating. Another set of pouch cells was cycled at various rates to quantify the energy efficiency improvements, with the charge and discharge curves shown in Figure S10. The LBCO cell has higher energy efficiency at every rate of charge (Figure S9), but a larger improvement is observed as the charging rate increases due to the smaller polarization. This increase in energy

efficiency has important implications for the amount of electrical energy (and associated emissions) required to replace petroleum in powering the vehicle fleet.
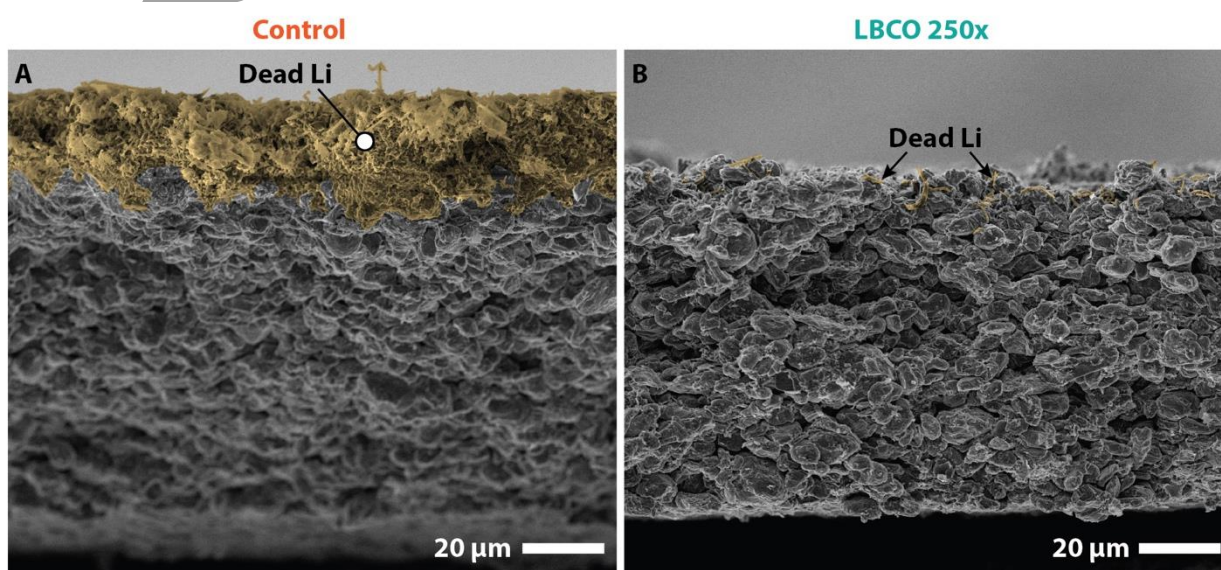
Pouch cells were also fabricated for the heated control, as well as cells with both the NMC and graphite electrode coated in 250x LBCO (Figure S11). The capacity retention of the heated controls is slightly better than the control, but exhibits a similar trend with a significant amount of Li plating. The cells with both the NMC and graphite coated with LBCO exhibit a slightly faster capacity fade than the cells with only the graphite coated. This suggests that the coating on the NMC is unnecessary for fast-charging when the graphite is coated. This is similar to the behavior observed previously for high voltage stability of ALD-coated electrodes,[32] and is consistent with the current understanding that the graphite electrode is the limiting factor for fast-charging in state-of-the-art LIBs.

To confirm that the initial capacity fade in the control was a result of Li plating, pouch cells were disassembled after 100 fast-charge cycles. As shown in **Figure 4a**, false-colored cross-sectional SEM images reveal a 20-30 μm thick layer of dead Li on the control electrode. A higher magnification image without false color is shown in Figure S12, which clearly shows the distinction between the round graphite particles and the porous dead Li layer. In contrast, the LBCO-coated electrode in Figure 4b exhibits only trace amounts of dead Li. The dead Li is formed due to irreversible stripping and re-intercalation of Li metal that nucleated and grew on the graphite surface.[54] This irreversibility depletes Li from the active reservoir, resulting in the capacity fading observed in Figure 3. In addition, the tortuous dead Li layer further impedes the mass transport in the cell during fast-charging and decreases rate performance.[55]

2.4. SEI impedance and the role in fast charging

The results from these pouch cells demonstrate that use of a single-ion conducting solid electrolyte with a wide electrochemical stability window as an a-SEI on graphite is a viable means to improve capacity retention under fast-charge conditions. To investigate the properties of the a-SEI further, we characterized the frequency-dependent impedance of the control and 250x LBCO electrodes using electrochemical impedance spectroscopy (EIS). EIS analysis was performed in a 3-electrode cell using a Li-metal ring reference electrode (further details in Experimental Methods). This enables us to deconvolute the contributions of each electrode to the total impedance. Since the impedance of various processes within LIBs is known to change significantly as a function of state-of-charge (SOC),[56,57] we collected impedance spectra at several points during charging of the cells.

Figure 4. Post mortem SEM images of graphite electrode cross-sections after 100 fast-

charge cycles for (A) uncoated control and (B) LBCO 250x.

Figure 5. Electrochemical impedance spectroscopy of graphite electrodes at various SOCs
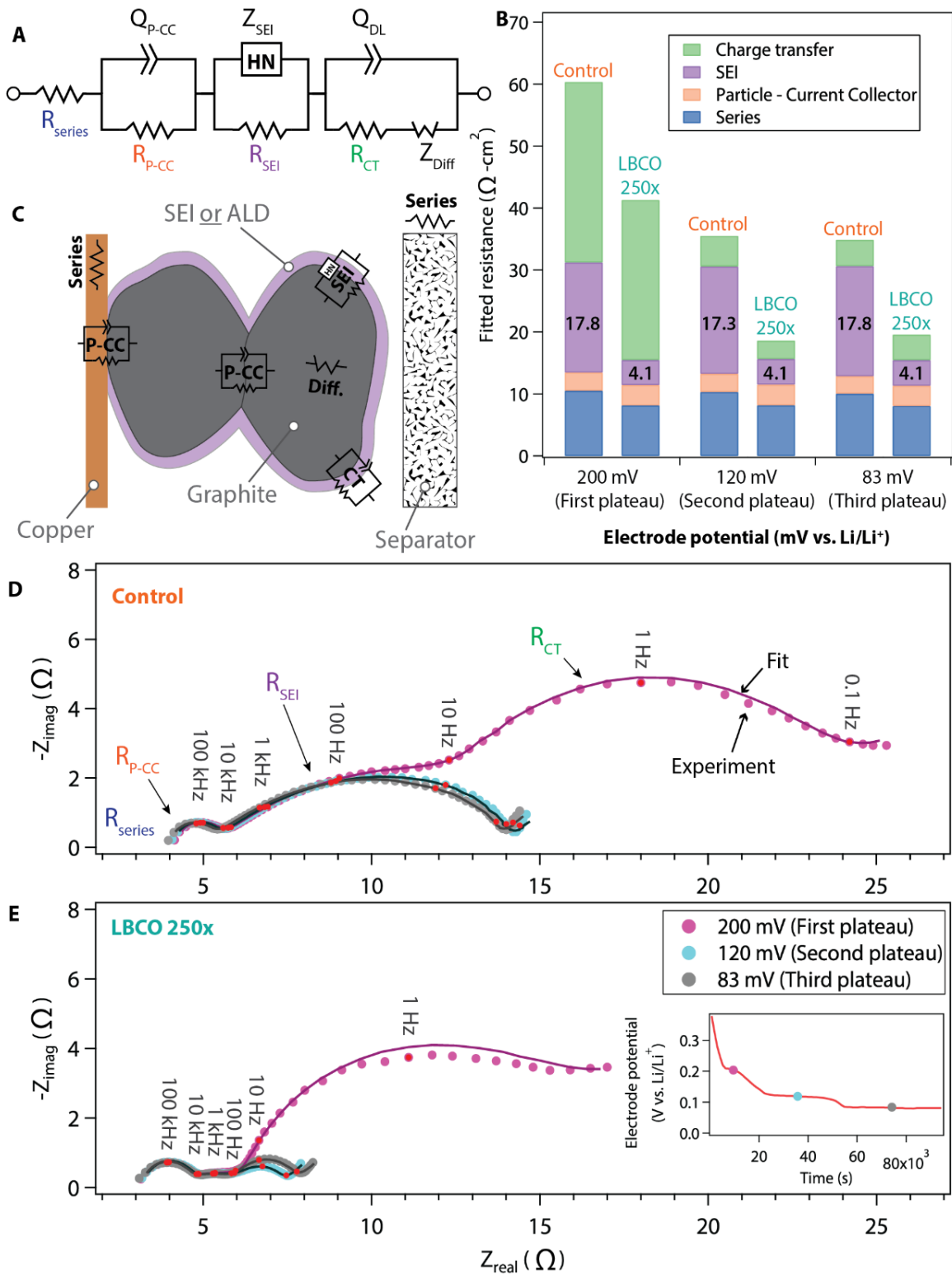
with/without LBCO ALD coating. (A) Equivalent circuit model that was used to fit the EIS spectra. (B) Stacked bar plot showing fitted resistance values for each resistance element of coated/uncoated electrodes at 3 different states of charge. Fitted resistances were multiplied by the area, 2.545 cm^2 to get area-specific resistances. (C) Schematic illustration of the origins of each circuit component in (A). Nyquist plots of uncoated control (D) and LBCO 250x (E) electrodes with selected frequencies labelled and marked by red dots and features labelled with their corresponding source based on the equivalent circuit model.

Contributions to the electrode impedance associated with distinct frequency responses were decoupled by fitting the spectra with the equivalent circuit model shown in **Figure 5d**. While there are numerous equivalent circuit models that have been implemented to fit LIB impedance spectra, the processes/features included are generally consistent (further details in Supplementary Information).[58]

The results, shown in Figure 5, exhibit some similarities between the control and LBCO 250x coated electrodes, but other key differences. Full details of the fitting results are shown in Table S3. In general, the series and contact resistances (R_{series} and R_{P-CC}) are similar for the two electrodes, and do not change substantially during charging. This is expected, as the origins of these impedances should not be significantly impacted by coating of the post-calendered electrode. In contrast, the charge-transfer resistance (R_{CT}) decreases with increasing SOC for both electrodes, consistent with previous reports.[56,59] This can be attributed to variations in the exchange current density as the concentration of Li in the electrode varies.[60]

The most substantial difference between the control and coated electrode is that the LBCO 250x has a significantly lower SEI resistance (R_{SEI}) than the control (4.1 Ω-cm^2 vs. 17.3-17.8 Ω-cm^2). This decreased SEI impedance can be rationalized by the facts that: 1) the LBCO coating successfully

19

suppressed natural SEI formation during charging; and 2) The LBCO a-SEI has a sufficiently high ionic conductivity and low electronic conductivity, both of which are stable across a wide range of electrochemical potentials.[29] The lower R_{SEI} reduces overall cell polarization, which is consistent with the voltage traces shown in Figure 3e.

Furthermore, at higher SOCs (120 mV and 83 mV), the lower R_{SEI} in the LBCO-coated electrode results in a decrease in the total impedance of the graphite electrode compared to the control by a factor of 48% and 44%, respectively. This is likely to have important implications during fast charging, because Li plating is known to occur on particles or local regions of the graphite electrode that are fully lithiated.[61,62]

The fact that the SEI resistance and composition (as measured by XPS, Figure 2) do not change measurably at various states of charge are indicative of the LBCO film remaining intact and functional, despite the volume changes expected in the graphite particles during cycling. This is also consistent with the continued suppression of Li plating over more than 500 cycles, which demonstrates that the ALD coatings provide a durable a-SEI under fast-charging conditions.

2.5. Delayed nucleation of Li plating

To further investigate the impact of the a-SEI on Li plating, a 3-electrode single-layer pouch cell with an integrated Li metal reference electrode was used to monitor the graphite electrode potential during fast charging (further details in Experimental Methods). **Figure 6a** shows both the anode potential (vs. Li/Li+) and total cell voltage during 4C charging at a constant current up to the 4.2 V cell voltage cutoff.

Consistent with the results above, the voltage curves are substantially different between the control and LBCO 250x electrodes. The control electrode potential (orange) quickly decreases, dropping below 0 V vs. Li/Li+ after just 3 minutes of charging (183 s). As the potential continues to decrease, the curve reaches a local minimum at around 400 s, and then begins increasing towards 0 V vs Li/Li+ before reaching a plateau. The LBCO 250x electrode potential decreases more slowly, remaining above 0 V vs Li/Li+ for 500 s, and does not reach a local minimum within the duration of the constant-current fast charging.
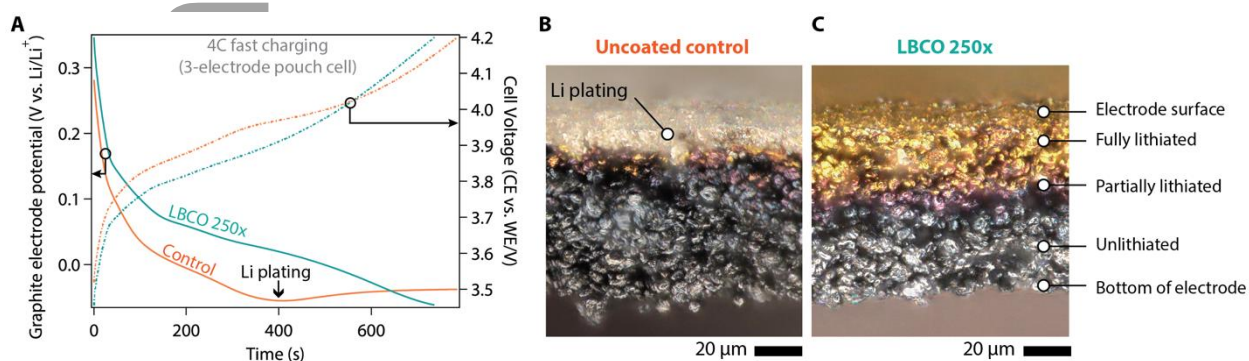

Figure 6. Fast-charging and Li plating in 3-electrode pouch cells. (A) Graphite electrode potential vs. Li/Li+ (graphite vs. reference) and cell voltage (NMC vs. graphite) during constant-current portion of 4C fast charging for control and LBCO 250x electrodes in 3-electrode single-layer pouch cells (B) Optical image of uncoated control graphite electrode cross-section after charging to 50% SOC at 4C in Li vs. graphite coin cell. (C) Same for LBCO 250x electrode.

The onset of Li plating has been correlated with the local minimum in the electrode potential during fast charging.[63] Because Li plating can only occur when the electrode potential drops below 0 V vs. Li/Li+, a more gradual potential drop during fast charging will delay the onset of

Li plating.[9] Thus, the more gradual voltage drop and lack of a local voltage minimum observed in the LBCO electrode are consistent with the suppression of Li plating.

To further explore the implications of the reduced polarization and its implications for Li plating during fast charging, 3-electrode pouch cells were charged at various rates from C/10 to 3C (Figure S13) . For 1C, 2C, and 3C, the LBCO 250x electrode potential remained above 0V vs. Li/Li+ for a significantly longer amount of time than in the control. This demonstrates that the amount of charge passed while the graphite electrode is below 0V vs. Li/Li+, and thus the driving force for Li plating, are significantly reduced by the LBCO a-SEI, consistent with the cycling results above.

The spatial distribution in SOC and Li plating on the graphite electrodes were visualized using *ex situ* optical microscopy. Similar to the 3-electrode cells, 2-electrode half-cells were charged at a 4C rate to 50% SOC. The cells were then immediately disassembled (within 1 minute) and imaged to observe the amount of Li plating and the gradient in SOC through the thickness of the electrode before the open-circuit rest period. Coin cells were used for these experiments, as they can be disassembled more rapidly to "freeze-in" any SOC gradients by removing the electrolyte.

The resulting images are shown in Figure 6b,c. As graphite is lithiated, there is a clear change in color, allowing for optical visualization of the local SOC distribution throughout the electrode.[64] On the control electrode, there is a large amount (~10 μm) of plated Li with a metallic luster on the top surface, and only a thin layer of fully-lithiated (gold colored) graphite underneath. This gradient in SOC is attributed to current focusing near the graphite/separator interface, which is typically attributed to mass transport limitations in the electrolyte.[5,9] In contrast, the LBCO 250x electrode has only trace amounts of plated Li and a the gold-colored graphite region extends further into the

electrode depth. This indicates that a larger fraction of the lithium was intercalated into the graphite during fast charging.

We attribute the suppression of Li plating and improved uniformity in the graphite SOC to the reduced SEI impedance of the coated electrode, as well as the improved homogeneity and stability of the a-SEI compared to the natural SEI. The reduced impedance makes the intercalation process more facile, requiring a lower overpotential and delaying the point at which the electrode potential drops below 0V vs. Li/Li$^+$. While the control electrode overpotential is large enough such that there is a sufficient driving force to nucleate Li metal, the LBCO electrode does not reach this condition during the 4C charge. Thus, while the a fraction of the charging current (and thus the Li flux) at the control graphite electrode is associated with Li plating, all of the Li flux in the LBCO electrode is associated with graphite intercalation. As a result, the total SoC of graphite in the LBCO electrode higher, and Li intercalation occurs deeper within the electrode volume during fast charging, as shown in Figure 6c.

We hypothesize that the improved chemical and structural homogeneity of the a-SEI itself at the nanoscale (compared to the natural SEI that forms without a coating) also plays a role in suppressing nucleation of Li during fast charging. An analogous effect occurs in Li metal electrodes, where chemical/structural heterogeneity of the SEI on can result in local current focusing along the electrode/electrolyte interface, which leads to a non-uniform Li flux and can induce mechanical stresses within the SEI.[65] The use of a uniform, amorphous coating that is reductively stable at low potentials as an a-SEI should prevent the formation of "hot-spots" that lead to preferential Li nucleation due to a high local current density. In contrast, the natural SEI is thought to be composed of a chemically/structurally inhomogenous mosaic, with local variations in ionic conductivity,

23

thickness, mechanical properties, and microstructure among the constituents. While a full mechanistic description of the spatial variations in current density will require follow-on modeling work, these observations highlight the potential for a pure surface modification to enable fast charging of graphite, despite the presence of electrolyte concentration gradients.

3. Conclusion

In this study, ALD was used to deposit a stable solid-state electrolyte as an a-SEI on graphite, which resulted in a significant improvement in fast-charging performance without sacrificing energy density. These results have led to several key findings:

1) LBCO a-SEI coatings can eliminate natural SEI formation during preconditioning. The LBCO-coated electrode has an SEI resistance of 4.1 Ω-cm^2, representing a four-fold reduction compared to the naturally formed SEI on the uncoated control electrode. This is possible because of the fact that LBCO is electrochemically stable (including at 0 V vs. Li/Li$^+$), and is composed of a single-ion conducting SE with a higher conductivity that the components of the natural SEI on graphite. The suppression of electrolyte decomposition and high ionic conductivity of the LBCO film also make it a promising candidate for use as an a-SEI on other electrode materials such as silicon, where a stable low-impedance interphase is also desirable.

2) Coating graphite with an a-SEI of LBCO dramatically reduces capacity fade during fast-charge cycling of pouch cells with commercially-relevant loadings. The a-SEI results in a significant improvement in cycle-life to 80% capacity retention with a 4C (15-min.) charging protocol (500 cycles, compared to just 12 for the uncoated control). This improved capacity retention is attributed to the suppression of Li plating. 3-electrode

measurements and post-mortem optical imaging shows that the decreased SEI impedance delays the onset of Li plating, which correlates with an improved uniformity of local SOC deeper within the electrode. In addition to improving Coulombic efficiency, the reduced cell polarization also increases the energy efficiency of the charging process.

3) The results of this study demonstrate that the SEI plays a key role in limiting fast-charging. To this point, the majority of fast-charging works have focused on improving mass transport in the liquid phase to enable faster rate charging. The present work challenges the idea that electrolyte transport must be improved to enable fast charging, and introduces an alternative strategy based only on interfacial modification of graphite. These observations highlight that while mass transport plays a major role, rational design of an optimized a-SEI also presents an opportunity to enhance fast-charging. Furthermore, since this is a fundamentally distinct approach, the results suggest a-SEI layers based on solid-state electrolytes could be combined with fast-charging strategies that utilize 3D architectures and new electrolyte compositions, enabling further improvements in extreme fast charging.

4. Experimental Section/Methods

Electrode Fabrication: Graphite and NMC electrodes were fabricated using the pilot scale roll-to-roll battery manufacturing facilities at the University of Michigan Battery Lab, as reported previously.[9] The graphite electrodes were fabricated with a total loading of 9.40 mg-cm^{-2} including 94% natural graphite (battery grade, SLC1506T, Superior Graphite), 1% C65 conductive additive, and 5% CMC/SBR binder), resulting in a theoretical capacity of 3.18 mAh-cm^{-2}. The specific surface area of the natural graphite specified by the manufacturer is 1.85 m^2/g, as measured by Brunauer–Emmett–

Teller (BET) method. The particle size distribution is shown in Figure S14. The electrodes were calendered to a porosity of ~32% (further details in Supporting Information). After coating, drying, calendaring, and punching, the full electrodes were transferred into an Veeco/Cambridge NanoTech Savannah S200 ALD reactor that is integrated into an argon glovebox for ALD coating.

$LiNi_{0.5}Mn_{0.3}Co_{0.2}O_2$ (battery grade, NMC-532, Toda America) was used as the cathode material. The cathode formulation was 92 wt.% NMC-532, 4 wt.% C65 conductive additive, and 4 wt.% PVDF binder. The cathode slurry was casted onto aluminum foils (15 μm thick) with a total areal mass loading of 16.58 mg-cm^{-2} and then calendered to 35% porosity. This yields an N:P ratio of 1.1-1.2.

Film Deposition and Characterization: The LBCO ALD film was deposited onto the electrodes using a modified version of the previously reported ALD process.[29] This process uses lithium tert-butoxide, triisopropyl borate, and ozone precursors. To ensure complete coverage of the high-surface-area electrode, the lithium tert-butoxide pulse length was increased to 10 s, with a 20 s exposure, and the triisopropyl borate pulse was increased to 0.25 s, with 20 s exposure. The deposition was conducted with a substrate temperature of 200 °C. Film thickness was measured on Si wafer pieces placed adjacent to the graphite electrodes using spectroscopic ellipsometry. A Woollam M-2000 was used to collect data, which were then fit with a Cauchy layer on top of the native oxide of the Si.

Film composition was characterized with X-ray photoelectron spectroscopy (XPS) using a Kratos Axis Ultra with monochromated Al Kα source. The XPS system is directly connected to an argon (Ar) glovebox to avoid all air exposure of samples. XPS data was analyzed with CasaXPS.

Binding energies were calibrated using the C-C peak in the C 1s core scan at 284.8 eV. The film and electrode morphology were characterized by scanning electron microscopy (SEM) using a Helios 650 nanolab dual beam SEM/FIB system. Electrode masses were measured using a Pioneer-series balance [Ohaus] inside an Argon glovebox, and electrode thicknesses were measured using an electronic thickness gauge (547-400S, Mitutoyo).

Cell Assembly: 2032 coin cells were assembled by punching circular electrodes from the larger pieces of ALD-coated and control electrodes. These electrodes were placed into the cells, followed by Entek EPH separator, 75 μL of electrolyte (1M LiPF$_6$ in 3:7 EC/EMC, Soulbrain MI), the NMC electrode, a stainless steel spacer, and a Belleville washer. Cells were crimped at a pressure of 1000 psi. Cells were tap charged to 1.5 V, and then allowed to rest for 12 hours to allow for electrolyte wetting. Three C/10 constant current preconditioning cycles were then performed on each cell using a cell cycler (Landt instruments) prior to other electrochemical characterization.

Pouch cell electrodes (7 cm x 10 cm) were punched and assembled into single-layer pouch cells in a dry room (< -40 °C dewpoint) at the University of Michigan Battery Laboratory. Each pouch cell consisted of an anode, a cathode, and a polymer separator (12 μm ENTEK). A N/P ratio of ~1.2 was fixed for all pouch cells. 3-electrode pouch cells incorporated a Au-coated Cu microwire between 2 layers of separator. Assembled dry cells were first baked in vacuum ovens at 50°C overnight to remove residual moisture prior to electrolyte filling. 1M LiPF$_6$ in 3/7 EC/EMC with 2% vinylene carbonate (SoulBrain MI) was used as the electrolyte. The vinylene carbonate additive has been shown to suppress alkyl decarbonate formation and enable superior cycling.[66] After electrolyte filling, pouch cells were vacuum-sealed and rested for 24 hours to allow for electrolyte wetting. Subsequently, two formation cycles were performed at C/20 and C/10 rates (one cycle for

This article is protected by copyright. All rights reserved.

27

each C-rate). After formation, cells were transferred back into the dry room, degassed, and then re-sealed prior to subsequent cycling.

Electrochemical Characterization: electrochemical impedance spectroscopy (EIS) was performed using an SP-200 or VSP potentiostat (Bio-logic USA). The spectra were fit to the equivalent circuit shown in Figure 5 using the RelaxIS 3® software suite (rhd instruments GmbH & Co. KG). 3-electrode EIS measurements were performed using a commercial electrochemical test cell (ECC-PAT-Core, EL-CELL GmbH) with a Li metal ring reference electrode. Preconditioning, rate tests, and fast-charge cycling were performed using a Maccor series 4000 cell cycler.

Post-mortem Characterization: XPS after preconditioning was performed as described above. Scanning electron microscopy and focused-ion beam milling was performed on a Helios G4 PFIB UXe (Thermo Fisher). The coin cells used for Figure 6b-c were disassembled using a disassembly die (MTI Corp.) as soon as possible after fast-charging was completed (within 1 minute). The electrodes were immediately rinsed in dimethyl carbonate to remove residual electrolyte and halt Li transport through the liquid phase. The electrodes were torn to create a cross-section, and then imaged with a VHX-7000 digital microscope (Keyence Corp.).

Acknowledgements

Author Contributions

Data Availability

All data generated or analysed during this study are included in the article and its Supplementary Information.

Conflict of Interest

The authors have filed a U.S. Patent application related to this work.

References

[1]   X. Zeng, M. Li, D. Abd El-Hady, W. Alshitari, A. S. Al-Bogami, J. Lu, K. Amine, *Adv. Energy Mater.* **2019**, *9*, 1900161.

[2]   J. Deng, C. Bae, A. Denlinger, T. Miller, *Joule* **2020**, *4*, 511.

[3]   K. G. Gallagher, S. E. Trask, C. Bauer, T. Woehrle, S. F. Lux, M. Tschech, P. Lamp, B. J. Polzin, S. Ha, B. Long, Q. Wu, W. Lu, D. W. Dees, A. N. Jansen, *J. Electrochem. Soc.* **2016**, *163*, A138.

[4]   Q. Liu, C. Du, B. Shen, P. Zuo, X. Cheng, Y. Ma, G. Yin, Y. Gao, *RSC Adv.* **2016**, *6*, 88683.

[5]   K. Chen, V. Goel, M. J. Namkoong, M. Wied, S. Müller, V. Wood, J. Sakamoto, K. Thornton, N. P. Dasgupta, *Adv. Energy Mater.* **2021**, *11*, 2003336.

[6]   C. P. Sandhya, B. John, C. Gouri, *Ionics (Kiel).* **2014**, *20*, 601.

[7]   K. J. Griffith, Y. Harada, S. Egusa, R. M. Ribas, R. S. Monteiro, R. B. Von Dreele, A. K. Cheetham, R. J. Cava, C. P. Grey, J. B. Goodenough, *Chem. Mater.* **2021**, *33*, 4.

[8]   J. B. Habedank, J. Kriegler, M. F. Zaeh, *J. Electrochem. Soc.* **2019**, *166*, A3940.

[9]   K.-H. Chen, M. J. Namkoong, V. Goel, C. Yang, S. Kazemiabnavi, S. M. Mortuza, E. Kazyak, J. Mazumder, K. Thornton, J. Sakamoto, N. P. Dasgupta, *J. Power Sources* **2020**, *471*, 228475.

[10]   L. Li, R. M. Erb, J. Wang, J. Wang, Y. M. Chiang, *Adv. Energy Mater.* **2019**, *9*, 1.

[11]   J. H. Shim, S. Lee, *J. Power Sources* **2016**, *324*, 475.

[12]   Q. Cheng, R. Yuge, K. Nakahara, N. Tamura, S. Miyamoto, *J. Power Sources* **2015**, *284*, 258.

[13]   X. G. Yang, T. Liu, Y. Gao, S. Ge, Y. Leng, D. Wang, C. Y. Wang, *Joule* **2019**, *3*, 3002.

[14]   D. S. Kim, D. J. Chung, J. Bae, G. Jeong, H. Kim, *Electrochim. Acta* **2017**, *258*, 336.

[15]   D. S. Kim, Y. E. Kim, H. Kim, *J. Power Sources* **2019**, *422*, 18.

[16]   K. R. Tallman, S. Yan, C. D. Quilty, A. Abraham, A. H. McCarthy, A. C. Marschilok, K. J. Takeuchi, E. S. Takeuchi, D. C. Bock, *J. Electrochem. Soc.* **2020**, *167*, 160503.

[17]   K. R. Tallman, B. Zhang, L. Wang, S. Yan, K. Thompson, X. Tong, J. Thieme, A. Kiss, A. C. Marschilok, K. J. Takeuchi, D. C. Bock, E. S. Takeuchi, *ACS Appl. Mater. Interfaces* **2019**, *11*, 46864.

[18]   X. Zhang, L. Zou, Y. Xu, X. Cao, M. H. Engelhard, B. E. Matthews, L. Zhong, H. Wu, H. Jia, X. Ren, P. Gao, Z. Chen, Y. Qin, C. Kompella, B. W. Arey, J. Li, D. Wang, C. Wang, J. G. Zhang, W. Xu, *Adv. Energy Mater.* **2020**, *10*, 1.

[19]   J. Shi, N. Ehteshami, J. Ma, H. Zhang, H. Liu, X. Zhang, J. Li, E. Paillard, *J. Power Sources* **2019**, *429*, 67.

[20]   Z. Du, D. L. Wood, I. Belharouak, *Electrochem. commun.* **2019**, *103*, 109.

[21]   E. Peled, D. Golodnitsky, G. Ardel, *J. Electrochem. Soc.* **1997**, *144*, L208.

[22]   E. Peled, *J. Electrochem. Soc.* **1979**, *126*, 2047.

[23]   D. Aurbach, B. Markovsky, I. Weissman, E. Levi, Y. Ein-Eli, *Electrochim. Acta* **1999**, *45*, 67.

[24]   K. Xu, *Chem. Rev.* **2014**, *114*, 11503.

[25]   Z. Zhang, Y. Shao, B. Lotsch, Y. S. Hu, H. Li, J. Janek, L. F. Nazar, C. W. Nan, J. Maier, M. Armand, L. Chen, *Energy Environ. Sci.* **2018**, *11*, 1945.

[26]   K. N. Wood, M. Noked, N. P. Dasgupta, *ACS Energy Lett.* **2017**, *2*, 664.

[27]   E. Kazyak, K.-H. Chen, A. L. Davis, S. Yu, A. J. Sanchez, J. Lasso, A. R. Bielinski, T. Thompson, J. Sakamoto, D. J. Siegel, N. P. Dasgupta, *J. Mater. Chem. A* **2018**, *6*, 19425.

[28]   E. Kazyak, K.-H. Chen, K. N. Wood, A. L. Davis, T. Thompson, A. R. Bielinski, A. J. Sanchez, X. Wang, C. Wang, J. Sakamoto, N. P. Dasgupta, *Chem. Mater.* **2017**, *29*, 3785.

[29]   E. Kazyak, K. H. Chen, A. L. Davis, S. Yu, A. J. Sanchez, J. Lasso, A. R. Bielinski, T. Thompson, J. Sakamoto, D. J. Siegel, N. P. Dasgupta, *J. Mater. Chem. A* **2018**, *6*, 19425.

[30]   S. H. Jung, K. Oh, Y. J. Nam, D. Y. Oh, P. Brüner, K. Kang, Y. S. Jung, *Chem. Mater.* **2018**, *30*, 8190.

[31]   S. M. George, *Chem. Rev.* **2010**, *110*, 111.

[32]   Y. S. Jung, P. Lu, A. S. Cavanagh, C. Ban, G. H. Kim, S. H. Lee, S. M. George, S. J. Harris, A. C. Dillon, *Adv. Energy Mater.* **2013**, *3*, 213.

[33]   Y. S. Jung, A. S. Cavanagh, L. A. Riley, S.-H. Kang, A. C. Dillon, M. D. Groner, S. M. George, S.-H. Lee, *Adv. Mater.* **2010**, *22*, 2172.

[34] M. L. Lee, C. Y. Su, Y. H. Lin, S. C. Liao, J. M. Chen, T. P. Perng, J. W. Yeh, H. C. Shih, *J. Power Sources* **2013**, *244*, 410.

[35] J. Liu, D. Lu, J. Zheng, P. Yan, B. Wang, X. Sun, Y. Shao, C. Wang, J. Xiao, J. G. Zhang, J. Liu, *ACS Appl. Mater. Interfaces* **2018**, *10*, 21965.

[36] K. Yan, H.-W. Lee, T. Gao, G. Zheng, H. Yao, H. Wang, Z. Lu, Y. Zhou, Z. Liang, Z. Liu, S. Chu, Y. Cui, *Nano Lett.* **2014**, *14*, 6016.

[37] X. Meng, X.-Q. Yang, X. Sun, *Adv. Mater.* **2012**, *24*, 3589.

[38] X. Wang, G. Yushin, *Energy Environ. Sci.* **2015**, *8*, 1889.

[39] L. Ma, R. B. Nuwayhid, T. Wu, Y. Lei, K. Amine, J. Lu, *Adv. Mater. Interfaces* **2016**, *3*.

[40] K. Dahlberg, J. E. Trevey, A. Dameron, H. M. Meyer III, R. E. Ruther, D. L. Wood III, L. Stevenson, D. Townsend, *ECS Meet. Abstr.* **2017**.

[41] Y. S. Jung, A. S. Cavanagh, A. C. Dillon, M. D. Groner, S. M. George, S. H. Lee, *J. Electrochem. Soc.* **2010**, *157*, 75.

[42] K. Wu, W. Li, J. Qin, Y. Hao, H. M. Kheimeh Sari, H. Feng, X. Li, *J. Mater. Res.* **2020**, *35*, 762.

[43] J. Liu, X. Sun, *Nanotechnology* **2015**, *26*, 024001.

[44] Y. Zhao, K. Zheng, X. Sun, *Joule* **2018**, *2*, 2583.

[45] H.-Y. Wang, F.-M. Wang, *J. Power Sources* **2013**, *233*, 1.

[46] I. D. Scott, Y. S. Jung, A. S. Cavanagh, Y. Yan, A. C. Dillon, S. M. George, S.-H. Lee, *Nano Lett.*

2011, *11*, 414.

[47] S. Leroy, F. Blanchard, R. Dedryvère, H. Martinez, B. Carré, D. Lemordant, D. Gonbeau, *Surf. Interface Anal.* **2005**, *37*, 773.

[48] D. L. Wood, J. Li, C. Daniel, *J. Power Sources* **2015**, *275*, 234.

[49] D. Strmcnik, I. E. Castelli, J. G. Connell, D. Haering, M. Zorko, P. Martins, P. P. Lopes, B. Genorio, T. Østergaard, H. A. Gasteiger, F. Maglia, B. K. Antonopoulos, V. R. Stamenkovic, J. Rossmeisl, N. M. Markovic, *Nat. Catal.* **2018**, *1*, 255.

[50] C. J. Powell, A. Jablonski, *J. Surf. Anal.* **2002**, *9*, 322.

[51] J. P. Christopherson, *Battery Test Manual for Electric Vehicles*, **2015**.

[52] T. Waldmann, B. I. Hogg, M. Wohlfahrt-Mehrens, *J. Power Sources* **2018**, *384*, 107.

[53] M. Petzl, M. Kasper, M. A. Danzer, *J. Power Sources* **2015**, *275*, 799.

[54] J. Wandt, P. Jakes, J. Granwehr, R. A. Eichel, H. A. Gasteiger, *Mater. Today* **2018**, *21*, 231.

[55] K.-H. Chen, K. N. Wood, E. Kazyak, W. S. LePage, A. L. Davis, A. J. Sanchez, N. P. Dasgupta, *J. Mater. Chem. A* **2017**, *5*, 11671.

[56] C. Wang, A. J. Appleby, F. E. Little, *Electrochim. Acta* **2001**, *46*, 1793.

[57] M. Itagaki, S. Yotsuda, N. Kobari, K. Watanabe, S. Kinoshita, M. Ue, *Electrochim. Acta* **2006**, *51*, 1629.

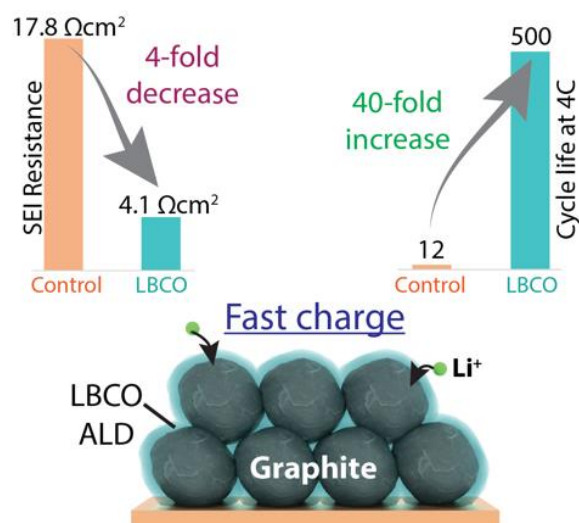[58] J. Illig, *Physically based impedance modelling of lithium-ion cells*, **2014**.

[59]   J. Illig, M. Ender, A. Weber, E. Ivers-Tiffée, *J. Power Sources* **2015**, *282*, 335.

[60]   P. Yu, J. A. Ritter, R. E. White, B. N. Popov, *J. Electrochem. Soc.* **2000**, *147*, 2081.

[61]   M. W. Verbrugge, D. R. Baker, *J. Phys. Energy* **2019**, *2*, 014004.

[62]   T. Gao, Y. Han, D. Fraggedakis, S. Das, T. Zhou, C. N. Yeh, S. Xu, W. C. Chueh, J. Li, M. Z. Bazant, *Joule* **2021**, *5*, 393.

[63]   C. Fear, T. Adhikary, R. Carter, A. N. Mistry, C. T. Love, P. P. Mukherjee, *ACS Appl. Mater. Interfaces* **2020**, *12*, 30438.

[64]   Y. Qi, S. J. Harris, *J. Electrochem. Soc.* **2010**, *157*, A741.

[65]   F. Hao, A. Verma, P. P. Mukherjee, *J. Mater. Chem. A* **2018**, *6*, 19664.

[66]   T. Sasaki, T. Abe, Y. Iriyama, M. Inaba, Z. Ogumi, *J. Electrochem. Soc.* **2005**, *152*, A2046.

This work demonstrates an artificial SEI coating with 75% lower impedance compared to the natural SEI. This coating enables stable cycling under 4C (15 min) charging conditions, retaining 80% capacity over 500 cycles. This challenges the prevailing assumption that mass transport limitations must be addressed to enable fast charging.

Eric Kazyak, Kuan-Hung Chen, Yuxin Chen, Tae H. Cho, Neil P. Dasgupta*

Enabling 4C Fast Charging of Lithium-ion Batteries with a Solid-State Electrolyte Coating